

# Metastable high-entropy dual-phase alloys overcome the strength–ductility trade-off

Zhiming Li<sup>1</sup>, Konda Gokuldoss Pradeep<sup>1</sup>, Yun Deng<sup>1</sup>, Dierk Raabe<sup>1</sup> & Cemal Cem Tasan<sup>1,2</sup>

Metals have been mankind's most essential materials for thousands of years; however, their use is affected by ecological and economical concerns. Alloys with higher strength and ductility could alleviate some of these concerns by reducing weight and improving energy efficiency. However, most metallurgical mechanisms for increasing strength lead to ductility loss, an effect referred to as the strength–ductility trade-off<sup>1,2</sup>. Here we present a metastability-engineering strategy in which we design nanostructured, bulk high-entropy alloys with multiple compositionally equivalent high-entropy phases. High-entropy alloys were originally proposed to benefit from phase stabilization through entropy maximization<sup>3–6</sup>. Yet here, motivated by recent work that relaxes the strict restrictions on high-entropy alloy compositions by demonstrating the weakness of this connection<sup>7–11</sup>, the concept is overturned. We decrease phase stability to achieve two key benefits: interface hardening due to a dual-phase microstructure (resulting from reduced thermal stability of the high-temperature phase<sup>12</sup>); and transformation-induced hardening (resulting from the reduced mechanical stability of the room-temperature phase<sup>13</sup>). This combines the best of two worlds: extensive hardening due to the decreased phase stability known from advanced steels<sup>14,15</sup> and massive solid-solution strengthening of high-entropy alloys<sup>3</sup>. In our transformation-induced plasticity-assisted, dual-phase high-entropy alloy (TRIP-DP-HEA), these two contributions lead respectively to enhanced trans-grain and inter-grain slip resistance, and hence, increased strength. Moreover, the increased strain hardening capacity that is enabled by dislocation hardening of the stable phase and transformation-induced hardening of the metastable phase produces increased ductility. This combined increase in strength

and ductility distinguishes the TRIP-DP-HEA alloy from other recently developed structural materials<sup>16,17</sup>. This metastability-engineering strategy should thus usefully guide design in the near-infinite compositional space of high-entropy alloys.

To realize the TRIP-DP-HEA concept, we switch from the equi-atomic  $\text{Fe}_{20}\text{Mn}_{20}\text{Ni}_{20}\text{Co}_{20}\text{Cr}_{20}$  (atomic per cent, at%)<sup>6</sup> system to the non-equiatomic  $\text{Fe}_{80-x}\text{Mn}_x\text{Co}_{10}\text{Cr}_{10}$  (at%) system, which exhibits partial martensitic transformation of the face-centred cubic (f.c.c.) to the hexagonal close-packed (h.c.p.) phase upon cooling from the high-temperature single-phase region. This change enables development of a dual-phase microstructure in which both phases obtain the maximum benefit of the solid-solution strengthening effect and one phase, owing to the decreased stacking fault energy<sup>18</sup>, undergoes deformation-induced displacive transformation. The partial martensitic transformation during quenching is the only possible approach that can lead to the formation of a DP-HEA with phases of identical chemical composition (that is, high-entropy phases). The alloys were synthesized with varying Mn contents in a vacuum induction furnace using pure metals, hot-rolled to 50% thickness at 900 °C, homogenized at 1,200 °C for 2 h in an Ar atmosphere, and water-quenched. Further grain refinement was achieved by cold-rolling (to 60% thickness) and 3-min annealing at 900 °C in an Ar atmosphere. The chemical composition of the HEAs measured by wet-chemical analysis is given in Extended Data Table 1.

Microstructure characterization down to 30-nm resolution reveals that the  $\text{Fe}_{80-x}\text{Mn}_x\text{Co}_{10}\text{Cr}_{10}$  (at%) system indeed demonstrates the targeted change in phase stability (see the X-ray diffraction (XRD) and electron backscatter diffraction (EBSD) data in Fig. 1). A single f.c.c. phase structure was obtained when the Mn content was 45 at% and 40 at% ( $\text{Fe}_{35}\text{Mn}_{45}\text{Co}_{10}\text{Cr}_{10}$  and  $\text{Fe}_{40}\text{Mn}_{40}\text{Co}_{10}\text{Cr}_{10}$ , respectively).

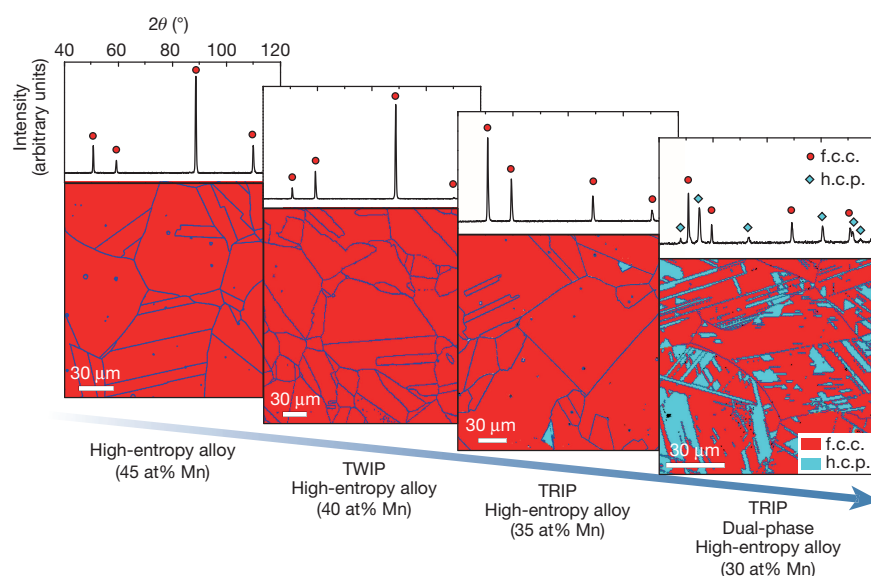


**Figure 1 | XRD patterns and EBSD phase maps of  $\text{Fe}_{80-x}\text{Mn}_x\text{Co}_{10}\text{Cr}_{10}$  ( $x = 45$  at%, 40 at%, 35 at% and 30 at%) HEAs.**  $\theta$  is the Bragg angle. The Mn content plays an important part in phase constitution, tuning phase stability for the activation of specific displacing transformation mechanisms, for example, enabling TWIP or TRIP effects. We note that the 35 at% Mn alloy has only trace amounts of the h.c.p. phase, and hence is not referred to as a DP-HEA.

<sup>1</sup>Max-Planck-Institut für Eisenforschung, Max-Planck-Straße 1, 40237 Düsseldorf, Germany. <sup>2</sup>Department of Materials Science and Engineering, Massachusetts Institute of Technology, 77 Massachusetts Avenue, Cambridge, Massachusetts 02139 USA.

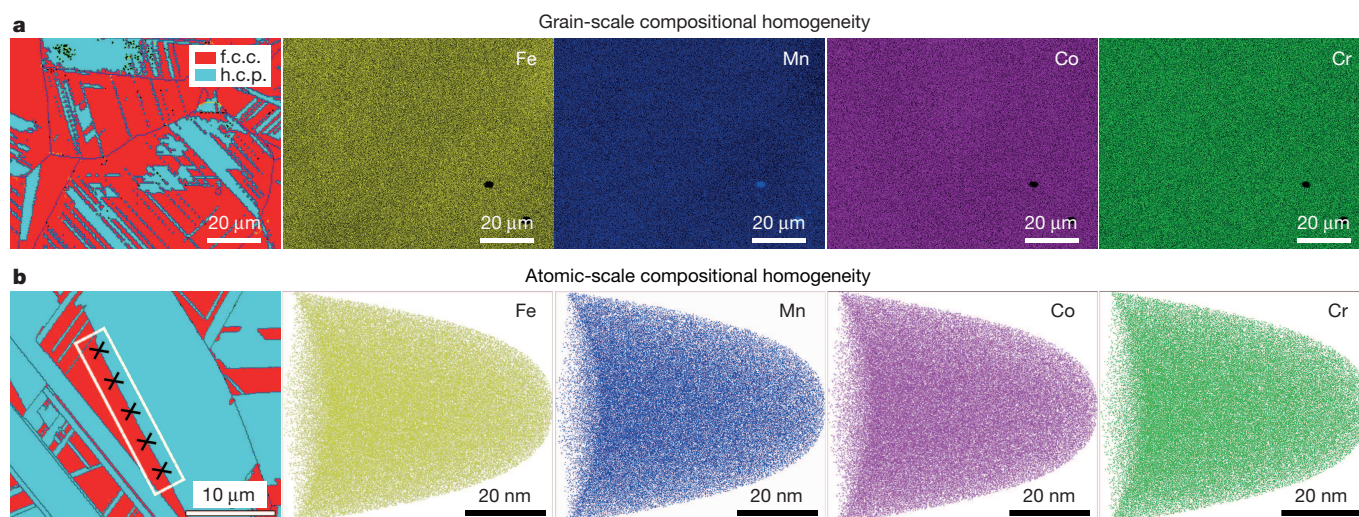


**Figure 2 | Elemental homogeneity among the two phases of  $\text{Fe}_{50}\text{Mn}_{30}\text{Co}_{10}\text{Cr}_{10}$  (at%) HEA.** **a**, Energy-dispersive spectroscopy maps of the shown EBSD-mapped sample region. **b**, Three-dimensional APT tip reconstructions of Fe, Mn, Co, Cr atom positions in a typical APT tip from the EBSD-mapped phase boundary. The crosses refer to the positions that the APT tips were taken from.

These two alloys demonstrate a transition in the deformation mechanisms from dislocation-dominated plasticity in the former<sup>8</sup> to twinning-induced plasticity (TWIP) in the latter<sup>10</sup>, confirming the targeted stability trend realized by tuning the stacking fault energy. A further decrease to 35 at% Mn leads to traces of h.c.p. phase (not captured by XRD). Finally, a decrease to 30 at% Mn ( $\text{Fe}_{50}\text{Mn}_{30}\text{Co}_{10}\text{Cr}_{10}$ ) successfully produces the desired dual-phase microstructure with  $\sim 28\%$  h.c.p. phase. This alloy is analysed in more detail in the following.

The two phases constituting the as-quenched  $\text{Fe}_{50}\text{Mn}_{30}\text{Co}_{10}\text{Cr}_{10}$  (at%) alloy are the f.c.c.  $\gamma$  matrix (of  $\sim 45\text{-}\mu\text{m}$  grain size) and the h.c.p.  $\epsilon$  phase laminate layers (ranging from several nanometres to  $10\text{-}\mu\text{m}$  in thickness). In Fig. 2, energy dispersive spectroscopy and atom probe tomography (APT) maps are also provided for the corresponding EBSD maps, respectively, to reveal the compositional distribution among the two phases. The energy dispersive spectroscopy maps in Fig. 2a show that all elements are uniformly distributed, suggesting that both phases benefit from the same level of solid solution strengthening. APT tips were lifted out from a phase boundary region (using the method outlined in ref. 19) shown in the EBSD phase map in Fig. 2b, to

rule out the possibility of atomic-scale elemental partitioning between the f.c.c. and the h.c.p. phases. The analysis reveals that the investigated volume has an overall composition of  $\text{Fe}_{48.6}\text{Mn}_{27.6}\text{Co}_{11.3}\text{Cr}_{12.3}$  (at%), showing values near the nominal bulk composition. No apparent elemental segregations can be observed in the three-dimensional reconstructions (Fig. 2b) or from the statistical binomial frequency distribution analyses (Extended Data Fig. 1), confirming the uniform distribution of all elements even at phase boundaries. This is different from Mn-containing steels, which show substantial chemical gradients across phase boundaries<sup>20,21</sup>.

Figure 3a shows the mechanical response of the DP-HEA for the coarse-grained (as-homogenized, grain size of  $\sim 45\text{-}\mu\text{m}$ ) and grain-refined (recrystallized, grain size of  $\sim 4.5\text{-}\mu\text{m}$ ) states. To emphasize the substantial improvement in the properties upon grain refinement, the curves for two other single-f.c.c.-phase HEAs ( $\text{Fe}_{37}\text{Mn}_{45}\text{Co}_9\text{Cr}_9$  (ref. 8) and  $\text{Fe}_{20}\text{Mn}_{20}\text{Ni}_{20}\text{Co}_{20}\text{Cr}_{20}$  (ref. 6) (at%)) are also presented.

The mechanical response of the TRIP-DP-HEA is striking even before grain refinement. It exhibits vastly higher strength and ductility compared to the single-phase  $\text{Fe}_{37}\text{Mn}_{45}\text{Co}_9\text{Cr}_9$  (at%) HEA. More

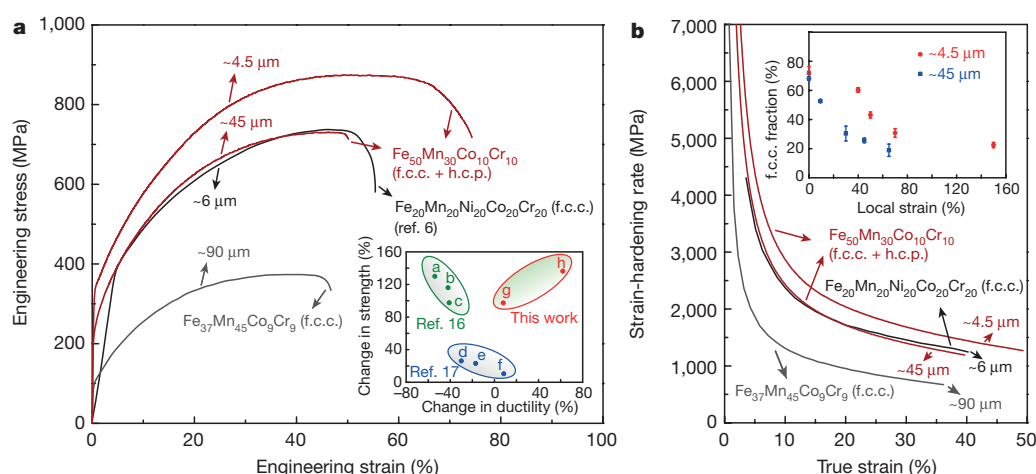


**Figure 3 | Mechanical behaviour of the TRIP-DP-HEAs compared to various single-phase HEAs.** Grain sizes are shown in micrometres. **a**, Tensile properties. The tensile-curve data of single-phase  $\text{Fe}_{20}\text{Mn}_{20}\text{Ni}_{20}\text{Co}_{20}\text{Cr}_{20}$  (at%) in ref. 6 is also shown here. The inset shows the increments of (change in) strength and ductility in refs 16 and 17 and this work; ultimate tensile strength and elongation to fracture were used as strength and ductility. Inset labels a, b and c represent the heterogeneous lamella Ti60, Ti80 and Ti100 versus coarse-grained Ti, respectively<sup>16</sup>; d, e and f represent the high-specific-strength steels I, II and III versus weight-reduced Fe-Al-Mn-C steel, respectively<sup>17</sup>; g and h represent the coarse-grained (grain size  $\sim 45\text{-}\mu\text{m}$ ) and grain refined (grain size  $\sim 4.5\text{-}\mu\text{m}$ ) DP-HEAs versus the single-phase  $\text{Fe}_{37}\text{Mn}_{45}\text{Co}_9\text{Cr}_9$  (at%) HEA, respectively. **b**, Strain-hardening response. The inset shows how the stability of the f.c.c. phase was optimized upon grain refinement to increase the strain-hardening ability; the data points in the inset are means  $\pm$  standard deviation of three tests.



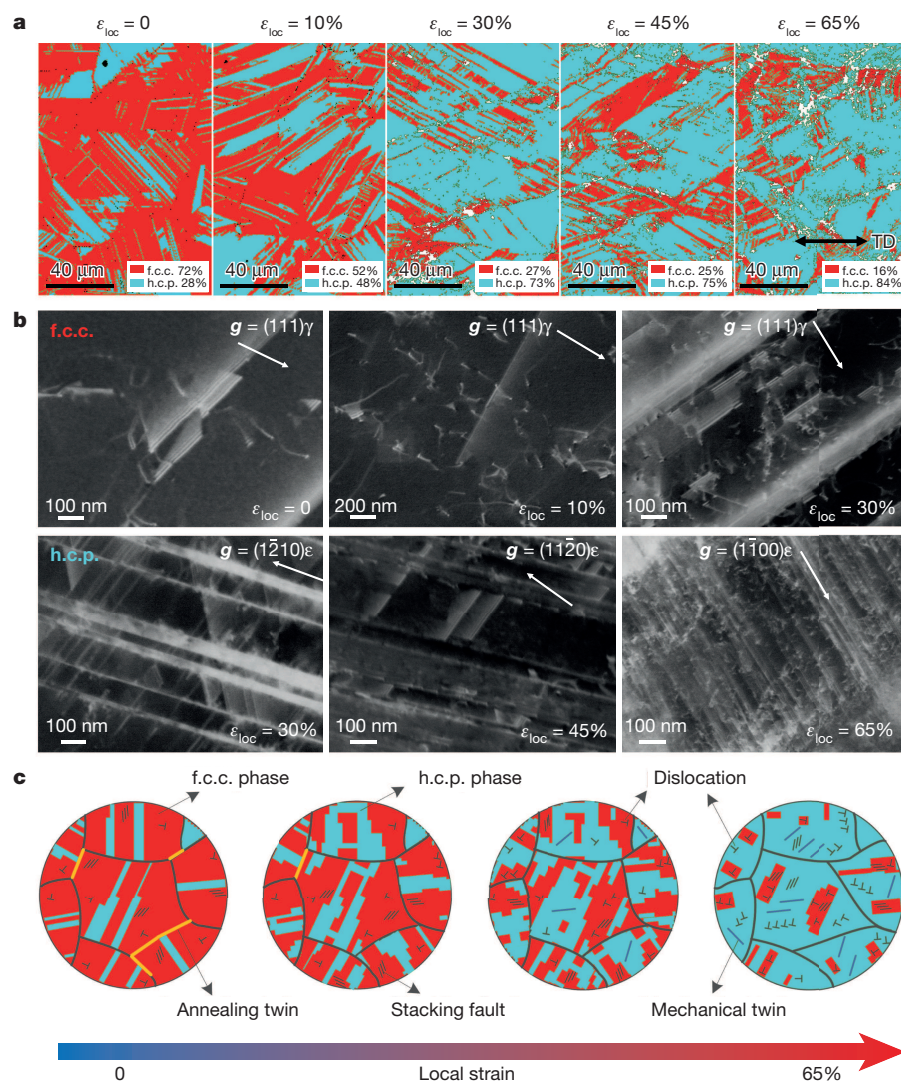


**Figure 4 | Deformation micro-mechanisms in the TRIP-DP-HEA with increasing tensile deformation at room temperature.** **a**, EBSD phase maps revealing the deformation-induced martensitic transformation as a function of deformation.  $\epsilon_{loc}$  is the local strain and TD is the tensile direction. **b**, ECCI analyses showing the evolution of defect substructures in the f.c.c. and h.c.p. phases.  $g$  is the diffraction vector,  $\gamma$  is the f.c.c. phase and  $\epsilon$  is the h.c.p. phase. **c**, Schematic sketches illustrating the sequence of micro-processes in the TRIP-DP-HEA.

importantly, it has a mechanical response almost identical to that of the (grain-refined) single-phase  $\text{Fe}_{20}\text{Mn}_{20}\text{Ni}_{20}\text{Co}_{20}\text{Cr}_{20}$  (at%), the most successful HEA so far<sup>6,22</sup>. On grain refinement, TRIP-DP-HEA notably outperforms the  $\text{Fe}_{20}\text{Mn}_{20}\text{Ni}_{20}\text{Co}_{20}\text{Cr}_{20}$  (at%) HEA. Furthermore, the inset in Fig. 3a demonstrates that this approach in TRIP-DP-HEA has the potential to lead to superior improvements in strength-ductility combinations compared to those obtained in other studies that focus on conventional low-entropy systems<sup>16,17</sup>. Here, the ductility improvements observed in metallic glass matrix composites<sup>23,24</sup> are not shown for comparison, since for these materials the absolute levels of uniform tensile elongation are very low (for example,  $<3\%$ )<sup>24</sup> even when improved.

We note that the TRIP-DP-HEA reported in this work was designed mainly with the aim of proof of the proposed principle. In our opinion, much more substantial improvements can be achieved following the principles proposed here, if the microstructures and compositions are optimized further. Figure 3b reveals that these improvements correspond to a higher work hardening rate in the DP-HEA  $\text{Fe}_{50}\text{Mn}_{30}\text{Co}_{10}\text{Cr}_{10}$  (at%) than in the single-phase HEAs. This contributes also to an extended uniform deformation process (Extended Data Fig. 2a). There is a notable difference between the strain hardening responses of the coarse-grained and grain-refined  $\text{Fe}_{50}\text{Mn}_{30}\text{Co}_{10}\text{Cr}_{10}$  (at%) HEAs, which is linked to the size dependence of the f.c.c. phase stability (see the inset in Fig. 3b).

These large improvements in the mechanical properties of the TRIP-DP-HEA arise from the underlying plastic accommodation and

hardening processes. By coupling EBSD (Fig. 4a) with electron channeling contrast imaging (ECCI<sup>25</sup>) (Fig. 4b), here we unravel these underlying processes for the case of the coarse-grained TRIP-DP-HEA (Fig. 4c).

We first focus on the f.c.c. phase. EBSD phase maps reveal that the f.c.c. phase is metastable, as desired. It exhibits deformation-stimulated martensitic transformation (f.c.c.  $\rightarrow$  h.c.p.) as a primary deformation mechanism (Fig. 4a). The importance of this mechanism in the observed hardening response can be assessed by comparing the two TRIP-DP-HEAs with different grain sizes: when the stability of the f.c.c. phase is optimized such that martensitic transformation is observed over an extended deformation regime (as for the grain-refined TRIP-DP-HEA; see inset of Fig. 3b), the overall ductility is increased (compare the grain-refined and coarse-grained TRIP-DP-HEAs in Fig. 3a).

The ECCI analysis reveals the evolution of the deformation substructure in the f.c.c. phase (Fig. 4b). Prior to deformation (local strain,  $\epsilon_{loc} = 0$ ), a large number of stacking faults is observed in the TRIP-DP-HEA. Stacking faults present in the f.c.c.  $\gamma$  phase are formed by gliding of Shockley partials of  $1/6\langle 112 \rangle$  Burgers vector<sup>26,27</sup>. These features constitute thin plates of h.c.p. structure (that is, several atomic monolayers of stacking faults). These thin h.c.p. plates have been shown to act as the nuclei of the  $\epsilon$  martensite phase<sup>27</sup>, which forms through the overlapping of stacking faults. The observed stacking faults in the undeformed HEA are initial faults that did not sufficiently coalesce to form the thermally induced h.c.p.  $\epsilon$  phase but are likely to act as phase-formation nuclei when subjected to externally applied mechanical loads.

At early stages of deformation, mechanically induced transformation from the f.c.c.  $\gamma$  phase to the h.c.p.  $\epsilon$  phase acts as the primary deformation mechanism (Fig. 4a). Since the stacking faults act as nuclei for the formation of the h.c.p.  $\epsilon$  phase, a large number of stacking faults are required in the f.c.c. phase to realize the transformation from f.c.c. to h.c.p. phase at this stage. This is well documented by ECCI, together with an increase in the dislocation density (see the  $\epsilon_{\text{loc}} = 10\%$  and  $\epsilon_{\text{loc}} = 30\%$  states in Fig. 4b). Thus, dislocation plasticity and martensitic transformation plasticity are both activated at similar deformation levels. The increased phase boundary density due to transformation creates additional obstacles of dislocation slip, thereby contributing to the strain hardening. With increasing strain, transformation from the f.c.c.  $\gamma$  to the h.c.p.  $\epsilon$  phase continues to be the dominant deformation mechanism, yet dislocation activity in the f.c.c.  $\gamma$  phase becomes more important. At 65% local strain (corresponding to the post-necking state, see Extended Data Fig. 2b), only  $\sim 16\%$  of the f.c.c. phase is retained (Fig. 4a).

We next focus on the h.c.p. phase. The TRIP-DP-HEA was water-quenched after homogenization at 1,200 °C, so the starting h.c.p.  $\epsilon$  phase is thermally induced by the martensitic transformation. Neither the thermally induced  $\epsilon$  regions nor the mechanically induced h.c.p. regions show notable deformation-induced features at low strain levels. Gradually, deformation-induced twinning was observed in the h.c.p.  $\epsilon$  phase as an important deformation mechanism (Fig. 4b). Thus, as the local strain increases to 30% and then to 45%, an increase in the density of both mechanical nano-twins and stacking faults is observed in the h.c.p. phase (Fig. 4b). The phenomenon of twinning in the deformation-induced h.c.p. martensite has also been observed in other types of alloys<sup>28</sup>. This mechanism contributes profoundly to strain hardening through the dynamic Hall–Petch effect. This means that the interface density, through the continuously formed twins, increases constantly<sup>29</sup>. Further increase of the deformation leads to the presence of a high density of dislocations (Fig. 4b). Thus, the h.c.p.  $\epsilon$  phase plays an important part in plastic accommodation and hardening at later stages of deformation via multiple deformation mechanisms (that is, dislocation slip, twinning and the formation of stacking faults).

These deformation micro-mechanisms (Fig. 4) and the impressive mechanical response (Fig. 3) confirm the success of this method of simultaneously achieving greatly improved strength (from massive solid solution strengthening and the increased interface density) and ductility (from dislocation-plasticity and transformation-induced hardening). The synergic deformation of the two phases leads to a highly beneficial dynamic strain–stress partitioning effect<sup>30</sup>; with a decreased likelihood of damage nucleation owing to their elastic compliance. Such damage resistance is absent in most dual-phase alloys with high mechanical contrast across their hetero-interfaces<sup>12</sup>.

Our effort to combine the best characteristics of steels and HEAs has led to the design of a new class of transformation-induced plasticity-assisted, dual-phase HEA. The originally proposed HEA concept has motivated enormous efforts to design new alloys, but few of the resulting alloys have shown properties that justify the increased alloying content, in contrast to the alloy presented here, which exhibits excellent strength–ductility combinations. We emphasize that this alloy design strategy is opposite in approach to that generally used in HEAs design: rather than focusing on phase stabilization and single-phase formation, we propose that phase metastability, and ductile multi-phase configurations should be important future research goals in this field.

**Online Content** Methods, along with any additional Extended Data display items and Source Data, are available in the online version of the paper; references unique to these sections appear only in the online paper.

**Received 2 November 2015; accepted 24 March 2016.**

**Published online 18 May 2016.**

1. Ritchie, R. O. The conflicts between strength and toughness. *Nature Mater.* **10**, 817–822 (2011).
2. Wei, Y. *et al.* Evading the strength–ductility trade-off dilemma in steel through gradient hierarchical nanotwins. *Nature Commun.* **5**, 3580 (2014).

3. Yeh, J. W. *et al.* Nanostructured high-entropy alloys with multiple principal elements: novel alloy design concepts and outcomes. *Adv. Eng. Mater.* **6**, 299–303 (2004).
4. Zhang, Y. *et al.* Microstructures and properties of high-entropy alloys. *Prog. Mater. Sci.* **61**, 1–93 (2014).
5. Gludovatz, B. *et al.* Exceptional damage-tolerance of a medium-entropy alloy CrCoNi at cryogenic temperatures. *Nature Commun.* **7**, 10602 (2016).
6. Gludovatz, B. *et al.* A fracture-resistant high-entropy alloy for cryogenic applications. *Science* **345**, 1153–1158 (2014).
7. Yao, M. J., Pradeep, K. G., Tسان, C. C. & Raabe, D. A novel, single phase, non-equiatomic FeMnNiCoCr high-entropy alloy with exceptional phase stability and tensile ductility. *Scr. Mater.* **72–73**, 5–8 (2014).
8. Tسان, C. C. *et al.* Composition dependence of phase stability, deformation mechanisms, and mechanical properties of the CoCrFeMnNi high-entropy alloy system. *JOM* **66**, 1993–2001 (2014).
9. Pradeep, K. G. *et al.* Non-equiatomic high entropy alloys: approach towards rapid alloy screening and property-oriented design. *Mater. Sci. Eng. A* **648**, 183–192 (2015).
10. Deng, Y. *et al.* Design of a twinning-induced plasticity high entropy alloy. *Acta Mater.* **94**, 124–133 (2015).
11. Wang, Y. P., Li, B. S. & Fu, H. Z. Solid solution or intermetallics in a high-entropy alloy. *Adv. Eng. Mater.* **11**, 641–644 (2009).
12. Tسان, C. C. *et al.* An overview of dual-phase steels: advances in microstructure-oriented processing and micromechanically guided design. *Annu. Rev. Mater. Res.* **45**, 391–431 (2015).
13. Herrera, C., Ponge, D. & Raabe, D. Design of a novel Mn-based 1 GPa duplex stainless TRIP steel with 60% ductility by a reduction of austenite stability. *Acta Mater.* **59**, 4653–4664 (2011).
14. Hadfield, R. A. Hadfield's manganese steel. *Science* **12**, 284–286 (1888).
15. Grässel, O., Krüger, L., Frommeyer, G. & Meyer, L. W. High strength Fe–Mn–(Al, Si) TRIP/TWIP steels development–properties–application. *Int. J. Plast.* **16**, 1391–1409 (2000).
16. Wu, X. *et al.* Heterogeneous lamella structure unites ultrafine-grain strength with coarse-grain ductility. *Proc. Natl Acad. Sci. USA* **112**, 14501–14505 (2015).
17. Kim, S.-H., Kim, H. & Kim, N. J. Brittle intermetallic compound makes ultrastrong low-density steel with large ductility. *Nature* **518**, 77–79 (2015).
18. Pierce, D. T. *et al.* The influence of manganese content on the stacking fault and austenite/ $\epsilon$ -martensite interfacial energies in Fe–Mn–(Al–Si) steels investigated by experiment and theory. *Acta Mater.* **68**, 238–253 (2014).
19. Mandal, S., Pradeep, K. G., Zaefferer, S. & Raabe, D. A novel approach to measure grain boundary segregation in bulk polycrystalline materials in dependence of the boundaries' five rotational degrees of freedom. *Scr. Mater.* **81**, 16–19 (2014).
20. Dmitrieva, O. *et al.* Chemical gradients across phase boundaries between martensite and austenite in steel studied by atom probe tomography and simulation. *Acta Mater.* **59**, 364–374 (2011).
21. Raabe, D. *et al.* Segregation engineering enables nanoscale martensite to austenite phase transformation at grain boundaries: a pathway to ductile martensite. *Acta Mater.* **61**, 6132–6152 (2013).
22. Otto, F. *et al.* The influences of temperature and microstructure on the tensile properties of a CoCrFeMnNi high-entropy alloy. *Acta Mater.* **61**, 5743–5755 (2013).
23. Hays, C., Kim, C. & Johnson, W. L. Microstructure controlled shear band pattern formation and enhanced plasticity of bulk metallic glasses containing in situ formed ductile phase dendrite dispersions. *Phys. Rev. Lett.* **84**, 2901 (2000).
24. Hofmann, D. C. *et al.* Designing metallic glass matrix composites with high toughness and tensile ductility. *Nature* **451**, 1085–1089 (2008).
25. Zaefferer, S. & Elhami, N.-N. Theory and application of electron channelling contrast imaging under controlled diffraction conditions. *Acta Mater.* **75**, 20–50 (2014).
26. Yakubtsov, I. A., Ariapour, A. & Perovic, D. D. Effect of nitrogen on stacking fault energy of f.c.c. iron-based alloys. *Acta Mater.* **47**, 1271–1279 (1999).
27. Brooks, J. W., Loretto, M. H. & Smallman, R. E. Direct observations of martensite nuclei in stainless steel. *Acta Metall.* **27**, 1839–1847 (1979).
28. Kim, C. P., Oh, Y. S., Lee, S. & Kim, N. J. Realization of high tensile ductility in a bulk metallic glass composite by the utilization of deformation-induced martensitic transformation. *Scr. Mater.* **65**, 304–307 (2011).
29. Lu, K., Lu, L. & Suresh, S. Strengthening materials by engineering coherent internal boundaries at the nanoscale. *Science* **324**, 349–352 (2009).
30. Wang, M. M., Tسان, C. C., Ponge, D., Dippel, A. C. & Raabe, D. Nanolaminate transformation-induced plasticity–twinning-induced plasticity steel with dynamic strain partitioning and enhanced damage resistance. *Acta Mater.* **85**, 216–228 (2015).

**Acknowledgements** This work is financially supported by the European Research Council under the EU's 7th Framework Programme (FP7/2007–2013)/ERC grant agreement 290998. The contributions of H. Springer, S. Zaefferer, M. Nellessen, M. Adamek and F. Schlüter are also gratefully acknowledged.

**Author Contributions** C.C.T. and D.R. designed the research; Z.L. was the lead experimental scientist of the study; K.G.P. and Y.D. performed some of the alloy design experiments; and Z.L. and C.C.T. wrote the paper. All authors discussed the results and commented on the manuscript.

**Author Information** Reprints and permissions information is available at [www.nature.com/reprints](http://www.nature.com/reprints). The authors declare no competing financial interests. Readers are welcome to comment on the online version of the paper. Correspondence and requests for materials should be addressed to D.R. ([d.raabe@mpie.de](mailto:d.raabe@mpie.de)), C.C.T. ([tasan@mit.edu](mailto:tasan@mit.edu)) or Z.L. ([zhiming.li@mpie.de](mailto:zhiming.li@mpie.de)).

## METHODS

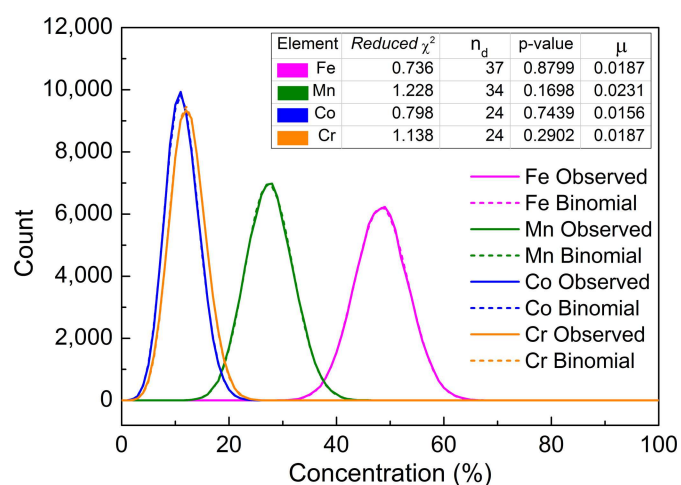
During the processing of the HEAs presented in this work, the ingot was first cast in a vacuum induction furnace using pure metals (purity higher than 99.8 wt%) with predetermined compositions. The as-cast ingot with dimensions of  $10 \times 50 \times 150 \text{ mm}^3$  was subsequently hot-rolled at  $900^\circ\text{C}$  with a rolling reduction ratio of 50% (thickness changed from 10 mm to 5 mm). After hot-rolling, the alloy was homogenized at  $1,200^\circ\text{C}$  for 2 h in an Ar atmosphere followed by water-quenching. For the  $\text{Fe}_{50}\text{Mn}_{30}\text{Co}_{10}\text{Cr}_{10}$  (at%) DP-HEA, further grain refinement was achieved through cold-rolling with a reduction ratio of 60% and subsequent recrystallization annealing at  $900^\circ\text{C}$  in an Ar atmosphere for 3 min followed by water-quenching. The bulk chemical compositions of all the studied alloys were measured by wet-chemical analysis (Extended Data Table 1).

The microstructures of the alloys were analysed using multiple techniques. EBSD measurements were performed using a Zeiss-Crossbeam XB 1540 focused ion beam scanning electron microscope (SEM) with a Hikari camera and the TSL OIM data-collection software (<http://www.edax.com/Products/EBSD/OIM-Data-Collection-EBSD-SEM.aspx>). Back-scattered electron imaging and ECCI<sup>25</sup> analyses were carried out using a Zeiss-Merlin instrument. The chemical uniformity

was investigated using energy-dispersive X-ray spectroscopy at the microscopic scale, and APT (LEAP 3000X HR, Cameca Inc.) at the atomic scale. The APT tips were produced using a focused ion beam (FEI Helios Nanolab 600i) from regions including phase and grain boundaries revealed by a prior EBSD scan.

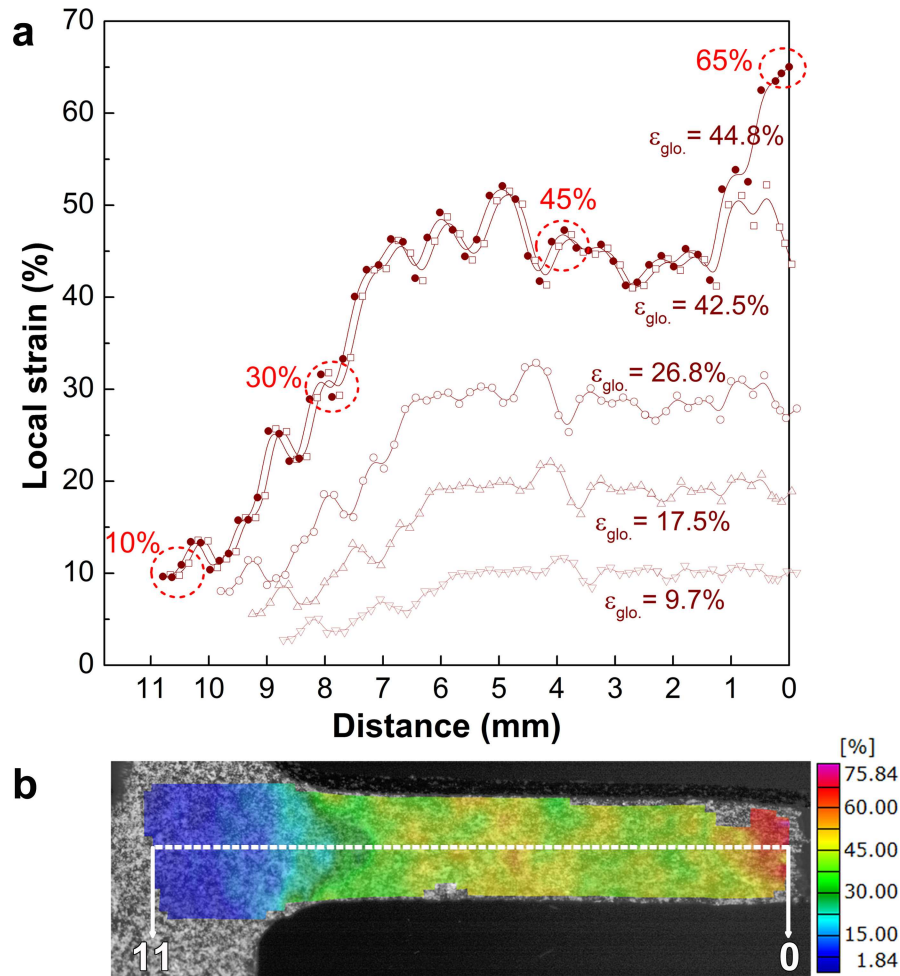
Flat specimens for tensile testing, with a thickness of 1 mm, were sectioned from the homogenized and water-quenched alloy by electrical discharge machining. The gauge length and width of the tensile specimens were 10 mm and 2.5 mm, respectively. Uniaxial tensile tests were carried out at ambient temperature using a Kammrath & Weiss tensile stage at the strain rate of  $1 \times 10^{-3} \text{ s}^{-1}$ . Five samples for each material were tensile-tested to confirm reproducibility. The local strain evolution during tensile test was determined by digital image correlation using the Aramis system (GOM GmbH, <http://www.gom.com/metrology-systems/system-overview/aramis.html>).

The deformation mechanisms in the DP-HEAs were investigated by EBSD and ECCI at different regions of the fractured tensile sample with different local strain levels. All of the sample regions analysed by ECCI were first measured by EBSD to obtain the specific orientation information corresponding to each region.



**Extended Data Figure 1 | Statistical binomial frequency distribution analysis results for the APT tip.** The statistical analysis shows that the tip has an overall composition of  $\text{Fe}_{48.6}\text{Mn}_{27.6}\text{Co}_{11.3}\text{Cr}_{12.3}$  (at%). The binomial curves obtained from the experiments match the curves corresponding to a total random distribution. The quality of the fit was quantified using several parameters, as listed in the key.  $n_d$  is the number of degrees of freedom for a given ion. The values of the normalized homogenization parameter  $\mu$  for all four elements are close to 0, confirming the random distribution of elements in the DP-HEA.





**Extended Data Figure 2 | Strain distribution within the DP-HEA sample upon room-temperature deformation. a,** Evolution of local strain with increasing the global strain ( $\epsilon_{\text{glo.}}$ ), indicating an extended uniform deformation process. The red dotted circles in **a** indicate the local strain values corresponding to various positions in the fractured tensile sample shown in **b**; four positions with local strains of 10%, 30%, 45%

and 65% were highlighted by percentages in red and the corresponding microstructures are shown in Fig. 4. **b,** Digital image correlation strain map shows the local strain distribution of the tensile sample following fracture. 0 to 11 in **b** refers to the distance of the sample position from the fracture surface, corresponding to the distance values shown in **a**.

Extended Data Table 1 | Chemical composition of the studied alloys in atomic per cent according to wet-chemical analysis

Alloy	Fe	Mn	Co	Cr
45%Mn	37.10	45.00	8.83	9.07
40%Mn	39.82	41.60	9.17	9.40
35%Mn	44.44	35.09	10.15	10.31
30%Mn	47.31	31.38	10.54	10.77